

Polarization-Independent Wavefront Manipulation of Surface Plasmons with Plasmonic Metasurfaces

Lin Chen,* Tangxuan Ren, Yang Zhao, Qiang Yu, Zengli Huang, Kai Zhang,* Jing Wen, Feng Lin,* and Shuqi Chen

Plasmonic metasurfaces show great potential to manipulate the wavefront of surface plasmons (SPs) and enable realization of various chip-level photonic devices. However, the current configurations can merely operate under specific incident polarization state and/or have limitation in independently tuning the phase and amplitude of SPs, although arbitrary incident polarization state is allowed. There is still the lack of a metasurface scheme that not only can couple spatial light waves into SPs under arbitrary polarization states, but also can independently modulate the amplitude and phase of the generated SPs. Here, it is proposed and experimentally demonstrated that double-lined metallic nanoslits can be well designed to overcome these limitations. Practical metadevices are designed and fabricated for generating polarization-independent plasmonic Airy beams, near-field focusing, and intensity-preserved “lossless” beams, and their excellent performances at 633 nm are characterized with near-field scanning optical microscope. The presented results will offer opportunities for the practical plasmonic devices and applications based on the plasmonic metasurfaces.

steps toward practical applications of SPs is to explore metadevices that not only can efficiently couple spatial light waves into SPs on metallic surfaces, but also can independently tune the amplitude and phase of the generated SPs. Generally, SPs excitation is restricted by the incidence polarization state due to the inherent electromagnetic nature of SPs. The widely used metallic gratings for SPs excitation require that the external light source polarizes along the grating period.^[4,5] Light in the orthogonal direction does not contribute to SP excitation, intrinsically resulting in substantial inconvenience and low excitation efficiencies for practical applications. In addition, the ever-increasing demand for generating complex SP field inevitably needs to independently modulate the phase and amplitude of SPs.

1. Introduction

As evanescent waves bound at a metal/dielectric interface, surface plasmons (SPs) can squeeze light field into a deep sub-wavelength scale, and have opened up a wide range of new opportunities in photonic research.^[1–3] One of the meaningful

Metasurfaces have recently provided a robust approach to control either free-space light or SPs via suitable spatial arrangement of well-designed plasmonic metasurfaces.^[6,7] As a common building block of plasmonic metasurfaces, a subwavelength metallic aperture has been extensively explored for SP excitation and wavefront manipulation. A variety of SP wavefront manipulation effects and

Prof. L. Chen, T. Ren
Wuhan National Laboratory for Optoelectronics
Huazhong University of Science and Technology
Wuhan 430074, China
E-mail: chen.lin@mail.hust.edu.cn


Y. Zhao, Prof. F. Lin
State Key Lab for Mesoscopic Physics
School of Physics
Peking University
Beijing 100871, China
E-mail: linf@pku.edu.cn

Q. Yu, Dr. K. Zhang
i-Lab
Suzhou Institute of Nano-Tech and Nano-Bionics (SINANO)
Chinese Academy of Sciences
Suzhou 215123, China
E-mail: kzhang2015@sinano.ac.cn

Dr. Z. Huang
Vacuum Interconnected Nanotech Workstation (Nano-X)
Suzhou Institute of Nano-Tech and Nano-Bionics (SINANO)
Chinese Academy of Sciences
Suzhou 215123, China

Prof. J. Wen
Engineering Research Center of Optical Instrument and System
Ministry of Education and Shanghai Key Laboratory
of Modern Optical System
University of Shanghai for Science and Technology
Shanghai 200093, China

Prof. S. Chen
The MOE Key Laboratory of Weak Light Nonlinear Photonics
School of Physics and TEDA Institute of Applied Physics
Nankai University
Tianjin 300071, China

 The ORCID identification number(s) for the author(s) of this article can be found under <https://doi.org/10.1002/adom.202000868>.

DOI: 10.1002/adom.202000868

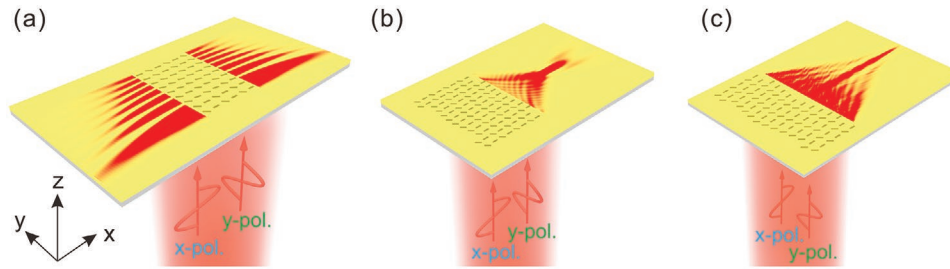


Figure 1. Double-lined metallic nanoslits for polarization-independent plasmonic a) Airy beam, b) near-field focusing, and c) intensity-preserved “lossless” beam.

applications have been demonstrated, including directional launching,^[8–10] Airy beams,^[4,11–14] near-field focusing,^[15–18] cosine-Gauss beam,^[19–22] and vortex beams.^[23–26] However, most of these configurations are polarization-sensitive since they can only convert spatial light waves into SPs under specific incident polarization state. A minority of design strategies can operate under arbitrary polarization states, but only have phase modulation.^[18,24] The absence of flexible amplitude modulation limits the capability of generating more complex SP field distributions, such as Airy beams, where both amplitude and phase modulation are required.

In this article, we show that well-designed double-lined metallic nanoslits can overcome the aforementioned limitations. The amplitude and phase of SPs can be independently controlled under arbitrary polarization states by appropriately arranging the rotation angles and the positions of nanoslits. In addition, one can readily boost the field intensity of SPs by simply increasing the number of the nanoslit columns. Three kinds of representative plasmon beams, including Airy beams (Figure 1a), near-field focusing (Figure 1b), and intensity-preserved “lossless” beams (Figure 1c), have been experimentally demonstrated, regardless of the incident polarization state.

2. Results and Discussions

2.1. Operating Principle

A single metallic nanoslit can be approximately seen as an in-plane magnetic dipole,^[9] where SPs can be excited merely if the incident light contains electric field component perpendicular to the long axis of the nanoslit (E_1 and E_2 in Figure 2a). When such nanoslits are distributed along the y direction with a spacing d smaller than the SP wavelength, the excited SPs are plane waves that travel away from the nanoslits with the propagation direction being perpendicular to the nanoslit column (along the x direction). By arranging the nanoslits in two lines spaced by a , the launched SPs from each column of the nanoslits will interfere with each other.^[8,9] Assuming a plane wave illuminates the paired nanoslits perpendicularly, the electric field can be expressed as

$$E_{\text{inc}} = A_x \vec{e}_x + A_y e^{i\phi} \vec{e}_y \quad (1)$$

where A_x and A_y are the amplitudes of the x - and y -components of the electric field, respectively, and ϕ represents the phase

difference between the x - and y -components. E_1 and E_2 can thus be expressed as

$$\begin{cases} E_1 = A_x \cos \theta_1 + A_y e^{i\phi} \sin \theta_1 \\ E_2 = A_x \cos \theta_2 + A_y e^{i\phi} \sin \theta_2 \end{cases} \quad (2)$$

where θ_1 and θ_2 are the rotation angles of the left and right nanoslits, respectively. Consider two points A (B) spacing from the right (left) column with b , as shown in Figure 2a. The superimposed electric field at A (B) contributed by the right and left column of nanoslits is proportional to E_R^A (E_R^B) and E_L^A (E_L^B)

$$\begin{cases} E_R^A = E_2 \cos \theta_2 e^{i(\beta_r + i\beta_i)b} \\ E_R^B = -E_2 \cos \theta_2 e^{i(\beta_r + i\beta_i)(b+a)} \end{cases} \quad (3)$$

$$\begin{cases} E_L^A = E_1 \cos \theta_1 e^{i(\beta_r + i\beta_i)(b+a)} \\ E_L^B = -E_1 \cos \theta_1 e^{i(\beta_r + i\beta_i)b} \end{cases} \quad (4)$$

where β_r and β_i denote the real and imaginary parts of the propagation constant of SPs, respectively. Considering that a is an infinitesimal as compared with the propagation length of SPs, the influence from the SP propagation loss can be ignored in Equations (3) and (4) ($e^{-\beta_i a} \approx 1$). The electric field component at A (B) is the superposition of E_R^A (E_R^B) and E_L^A (E_L^B), and can be simplified to

$$\begin{cases} E^A = E_R^A + E_L^A = [E_2 \cos \theta_2 e^{i\beta_r b} + E_1 \cos \theta_1 e^{i\beta_r(b+a)}] e^{-\beta_i b} \\ E^B = E_R^B + E_L^B = -[E_2 \cos \theta_2 e^{i\beta_r(b+a)} + E_1 \cos \theta_1 e^{i\beta_r b}] e^{-\beta_i b} \end{cases} \quad (5)$$

In the following study, we will focus on the electric field of SPs at A . Substituting Equation (2) into Equation (5) yields

$$E^A = \left[A_x (\cos^2 \theta_2 + \cos^2 \theta_1 e^{i\beta_r a}) + A_y e^{i\phi} (\sin \theta_2 \cos \theta_2 + \sin \theta_1 \cos \theta_1 e^{i\beta_r a}) \right] e^{i(\beta_r + i\beta_i)b} \quad (6)$$

where the first and the second terms in the square bracket arise from the x - and y -components of the electric field of the incident light, respectively. The polarization independency can be realized if the two terms inside the parentheses are equal

$$\cos^2 \theta_2 + \cos^2 \theta_1 e^{i\beta_r a} = \sin \theta_2 \cos \theta_2 + \sin \theta_1 \cos \theta_1 e^{i\beta_r a} \quad (7)$$

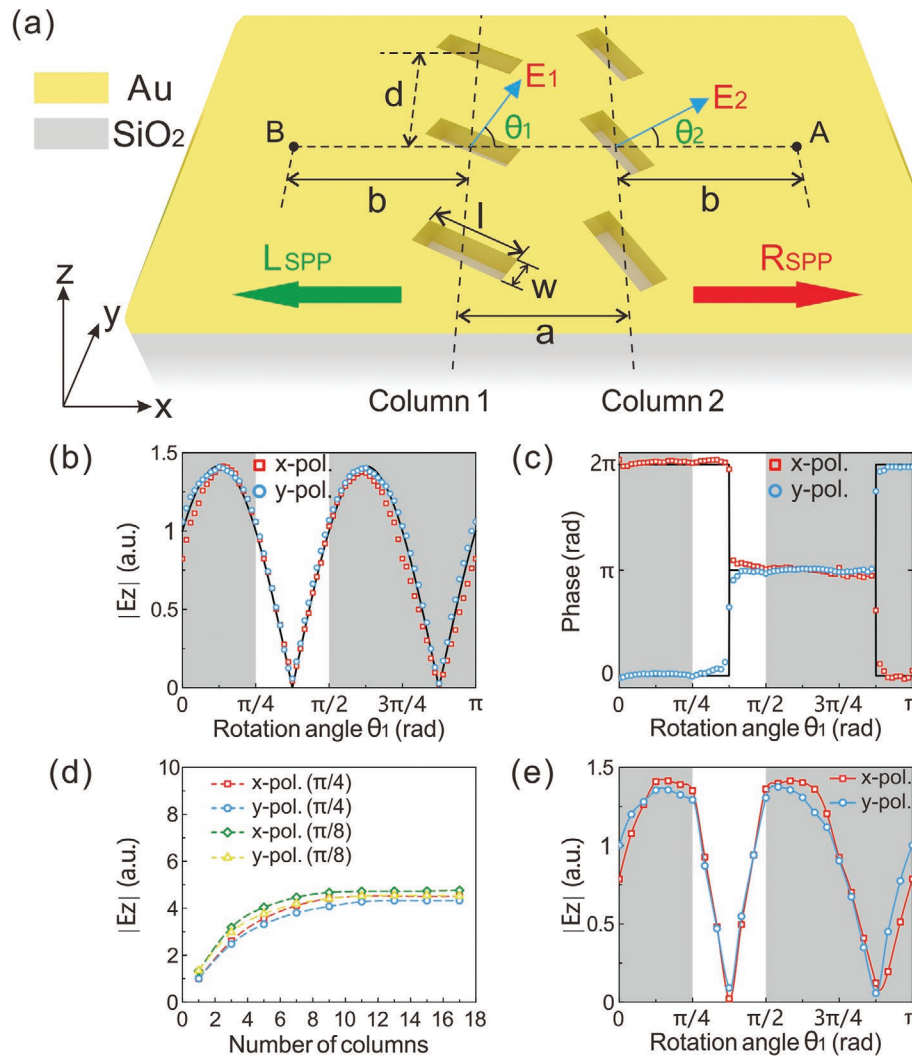


Figure 2. a) Schematic diagram of double-lined nanoslits with the rotation angles of θ_1 and θ_2 on a gold film. The period of the nanoslit segments along the y direction is d , and the distance between the two columns is a . b) The designed and simulated amplitude, represented by $\sqrt{2}|E_z|/\max(|E_z|)$, and c) phase of the SP electric field for the x and y polarizations at 633 nm versus θ_1 with $\theta_1 + \theta_2 = 3\pi/4$ for a single column of nanoslit pair. The black solid lines represent the designed values extracted from Equation (9). d) The simulated $\sqrt{2}|E_z|/\max(|E_z|)$ versus the number of nanoslit column pairs under the x - and y -polarized incidences, where θ_1 is set to be $\pi/4$ or $\pi/8$. e) The simulated $\sqrt{2}|E_z|/\max(|E_z|)$ for the x - and y -polarized incidences as a function of θ_1 , when the number of nanoslit column pairs is 13. In the simulations, $a = 305$ nm, $d = 300$ nm, $w = 60$ nm, and $l = 200$ nm are used, and the gold film is 150 nm thick.

Equation (7) can be satisfied only if $e^{i\beta a}$ is a real number (i.e., $e^{i\beta a} = 1$ or -1). If $e^{i\beta a} = 1$, Equation (6) is transformed to

$$E^A = (\cos^2\theta_2 + \cos^2\theta_1)(A_x + A_y e^{i\phi}) e^{i(\beta_x + i\beta_y)b} \quad (8)$$

The phase modulation is unachievable by changing θ_1 and θ_2 since we always have $\cos^2\theta_2 + \cos^2\theta_1 \geq 0$. If $e^{i\beta a} = -1$ ($a = (2N + 1)\pi/\beta$, N is a natural number), Equation (6) can be transformed to

$$E^A / (A_x + A_y e^{i\phi}) = -0.5(\cos 2\theta_1 + \sin 2\theta_1) e^{i(\beta_x + i\beta_y)b} \quad (9)$$

with $\theta_1 + \theta_2 = 3\pi/4$. The minimum value of a ($=\pi/\beta$) is chosen in the following work to achieve the maximum nanoslit density, thus increasing the excited SPPs intensity.

It should be noted here that the above equations can be derived on the prerequisite that the near-field coupling and scattering effects are ignored due to the sufficient spacing between adjacent nanoslits.^[12] To evaluate the influence of the near-field coupling or scattering effects on the generated SPP fields, we have simulated the SPPs field generated by the individual nanoslit column and the SPPs field in the presence of the two nanoslit columns. d is set at 300 nm by considering the tradeoff between the excited SPPs intensity and the fabrication difficulty (see the SPPs field intensity as a function of d in Figure S1, Supporting Information). The simulation results by finite difference time domain (FDTD) method with a commercial software FDTD Solutions clearly indicate that the linearly superposed SPPs fields excited by individual nanoslit columns match closely with the SPPs fields generated when both of the

two columns are present with $a = \pi/\beta_r$ (see Figure S2, Supporting Information). By changing θ_1 and θ_2 , the phase can suffer from a π shift, and the amplitude profile can follow a sine function. FDTD simulations are conducted to verify the amplitude and phase predicted by Equation (9). Figure 2b,c shows the amplitude represented by $\sqrt{2}|E_z|/\max(|E_z|)$, and the phase of the SP electric field at A, versus θ_1 with $\theta_1 + \theta_2 = 3\pi/4$, respectively, where the largest amplitude of E_z at $\theta_1 = \pi/8$ is represented by $\max(|E_z|)$. In the FDTD simulations, E_z is extracted at 10 nm above the metal surface and 10 μm away from the right nanoslit column. The simulated amplitude and phase of the SPs are well consistent with those predicted by Equation (9). To maximize the SP field intensity, we can as well increase the number of column pairs.^[8] By placing m column pairs with an interval of a SP wavelength on the left side of the nanoslit column presented in Figure 2a, the electric field intensity at A can be written as

$$E_{\text{total}}^A = \sum_{k=0}^m \left[E_2 \cos\theta_2 e^{i(\beta_r + i\beta_i)(b+k\lambda_{\text{sp}})} + E_1 \cos\theta_1 e^{i(\beta_r + i\beta_i)(b+a+k\lambda_{\text{sp}})} \right] \quad (10)$$

$$= \sum_{k=0}^m E^M e^{i(\beta_r + i\beta_i)k\lambda_{\text{sp}}} = E^M \left(\sum_{k=0}^m e^{-\beta_r k\lambda_{\text{sp}}} \right)$$

where λ_{sp} is the SP wavelength. Notably, the electric field intensity at A is enhanced with the increased number of column pairs. However, the growth rate is gradually reduced with the increase of the number of column pairs, which can be attributed to the fact that the SPs excited by the left column nanoslits have increased propagation distance from A, and hence undergo larger propagation loss. Figure 2d clearly illustrates that the field intensity at A eventually approaches a constant value for both x - and y -polarized incidences with $\theta_1 = \pi/8$ and $\pi/4$. This conclusion also applies to the field intensity at other θ_1 , which is not shown here. It should be noted that the electric field intensity shows gentle variation in the range of $\theta_1 \in [\pi/8, \pi/4]$ and $\theta_1 \in [\pi/2, 5\pi/8]$, if more column pairs are used. This can be verified by Figure 2e, which clearly shows the electric field intensity in the range of $\theta_1 \in [\pi/8, \pi/4]$ and $\theta_1 \in [\pi/2, 5\pi/8]$ changes smoothly, as compared to that in the remaining angle region. As a result, we have simply used the angle range of $\theta_1 \in [\pi/4, \pi/2]$ to enable the polarization-independent functionalities presented in Figure 1.

2.2. Design, Fabrication, and Measurement of Plasmonic Metadevices

Airy beams, analogous to Airy wave-packet solution for a free particle derived from the free particle Schrödinger equation in electromagnetism,^[27–29] have aroused considerable research interest owing to their intriguing diffraction-free, self-accelerating, and self-healing properties.^[29,30] Plasmonic Airy beams have great potential for energy routing in plasmonic circuits or surface particle manipulation.^[31] The truncated 1D Airy function can be described as

$$f(\xi) = \text{Airy}(\xi) \exp(\alpha\xi) \quad (11)$$

where $\xi = y/y_0$ represents the dimensionless transverse coordinate, y_0 is the transverse scale, and α is a positive value to ensure truncated Airy beams. The phase profile of the truncated Airy function is introduced, i.e., 0 phase for $f(\xi) > 0$ and π phase shift for $f(\xi) < 0$. The used amplitude and phase profiles are plotted in Figure 3a,b, respectively, which can be fulfilled by tuning θ_1 and θ_2 . The detailed values of θ_1 and θ_2 used in paired nanoslits along the y direction can be found in Figure S3, Supporting Information. The generated beam intensity can be enhanced by taking more nanoslit columns to couple light source into SPs. The field enhancement of Airy beams versus the number of nanoslit column pairs is shown in Figure 3c, where the field enhancement is defined as the ratio of the maximum electric field intensity 10 μm away from the rightmost nanoslits to that of the incident light. We can see the increasing field intensity discrepancies among different polarized incidences as the column number increases, which can be explained as follows. To generate Airy beams, the rotation angles of the nanoslits along the y direction should vary to fulfill the amplitude and phase profile required by Airy beams. This will render that a small amount of E_y component exists in the region of Airy beams, though the dominant electric field is still E_x and E_z . Different polarization incidences more or less generate distinct E_x , E_y , and E_z , and therefore lead to some field intensity discrepancies. Although the field enhancement reaches its maximum value at around 27 pairs of nanoslit column, we have merely used 17 pairs to implement the experiment by considering the fabrication complexities of more column pairs in focused ion beam (FIB) milling process. Compared with one pair of nanoslit column, the average electric field intensity with the x and y polarization incidences is increased by 50-folds with 17 pairs of nanoslit column.

The experimental fabrication of the plasmonic Airy beams was implemented by depositing a 150 nm-thick gold film via electron-beam vapor deposition on silica substrate. The pre-designed nanoslit pattern was formed by using FIB, and the scanning electron microscopy (SEM) image of the fabricated sample is shown in Figure 3d. A near-field scanning optical microscope (NSOM) in collection mode is used to measure the SP field distributions on the gold surface (Figure 3e). The sample is back-illuminated with a 633 nm He–Ne laser. The polarization of the incident beam can be flexibly switched among x , y , left circular, and right circular polarizations when it passes through a linear polarizer (LP) and a quarter-wave plate (QWP), and finally reaches the sample. An objective lens (10 \times , numerical aperture: 0.25) is used to slightly focus the normal-incident light onto the sample from the back. Figure 3f–i shows the simulated electric field intensity distributions under x -polarized, y -polarized, left circular polarized (LCP), and right circular polarized (RCP) incidences, respectively. It can be observed that Airy beams can be generated under arbitrary polarization states, and their field intensity distributions almost coincide. The measured electric field intensity distributions shown in Figure 3j–m basically agree with the simulated results.

Self-accelerating and nondiffraction features are the two key properties of Airy beams, which can be indicated by the variation of the deflection offset and the full width at half maximum (FWHM) of the main lobes, respectively. The deflection offsets

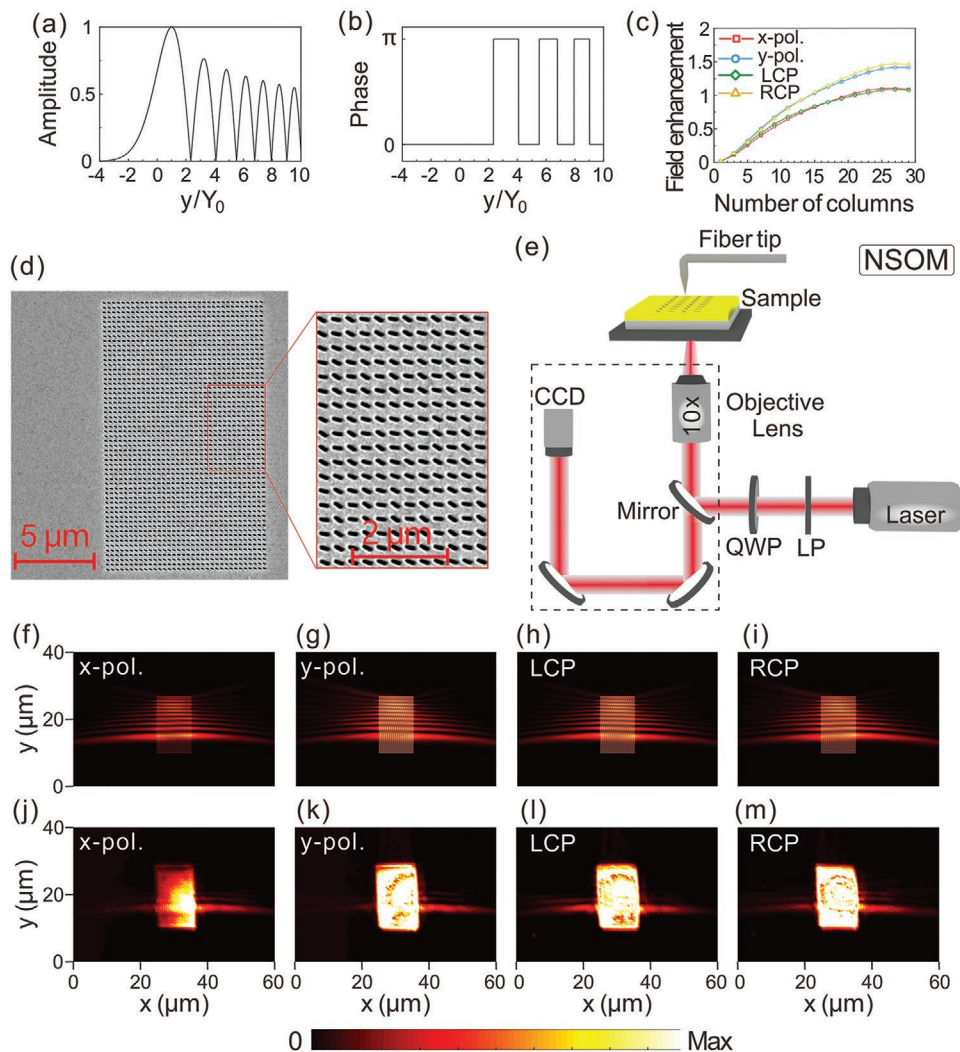


Figure 3. a) The amplitude and b) phase profile for the truncated Airy function with $\alpha = 0.005$ and $y_0 = 1 \mu\text{m}$. c) Simulated electric field intensity enhancement versus the number of nanoslit column pairs, under the x-polarized, y-polarized, LCP, and RCP incidences. d) SEM image of the sample for generating plasmonic Airy beams. e) Schematic diagram of the experimental setup with NSOM. f–m) Simulated (f–i) and NSOM-measured (j–m) electric field intensity distributions for the f,j) x-polarized, g,k) y-polarized, h,l) LCP, and i,m) RCP incidences, respectively.

of the plasmonic Airy beams extracted from the numerical and experimental results are basically in accordance with the theoretical prediction under different polarization states (see Figure S4a–d, Supporting Information). Meanwhile, the FWHM oscillates around the predesigned value of $1.64 \mu\text{m}$ and is almost kept below $2.46 \mu\text{m}$ (1.5 times of the predesigned value) even if the propagation distance reaches $40 \mu\text{m}$, regardless of the polarization states (see Figure S5a–d, Supporting Information). These results prove that the generated plasmonic Airy beams have very good performances under different polarization incidences.

As a counterpart of optical lens in the free space, near-field focusing plays an indispensable role in subwavelength focusing and performing SPP Fourier transform on a chip. The phase profile along the y direction for plasmonic focusing can be described as

$$\varphi(y) = \left(2\pi/\lambda_{\text{spp}}\right) \left(-\sqrt{y^2 + f^2} + f\right) + 2n\pi \quad (12)$$

where f represents the focal length, and n is an arbitrary integer. The designed phase profile desired is plotted in **Figure 4a**. There are 35 columns of nanoslits along the y direction, and the phase shift of each column is modulated by tuning the lateral distance with respect to the central column. The rightmost nanoslit of the central column along the y direction has a distance of $f = 10 \mu\text{m}$ from the focal point, where the SP intensity reaches the maximum value in the observation regions, and the lateral distances of each column along the y direction (with respect to the central column along the y direction) can be seen in Figure S6, Supporting Information. The field enhancement at the focal point increases with the nanoslit column pairs along the x direction, but the growth rate reduces (Figure 4b), where the field enhancement is defined as the ratio of the electric field intensity at the focal point to that of the incident light. Eleven nanoslit column pairs are used to implement the experiment and the field intensity at the focal point has 38-fold increase, in contrast to

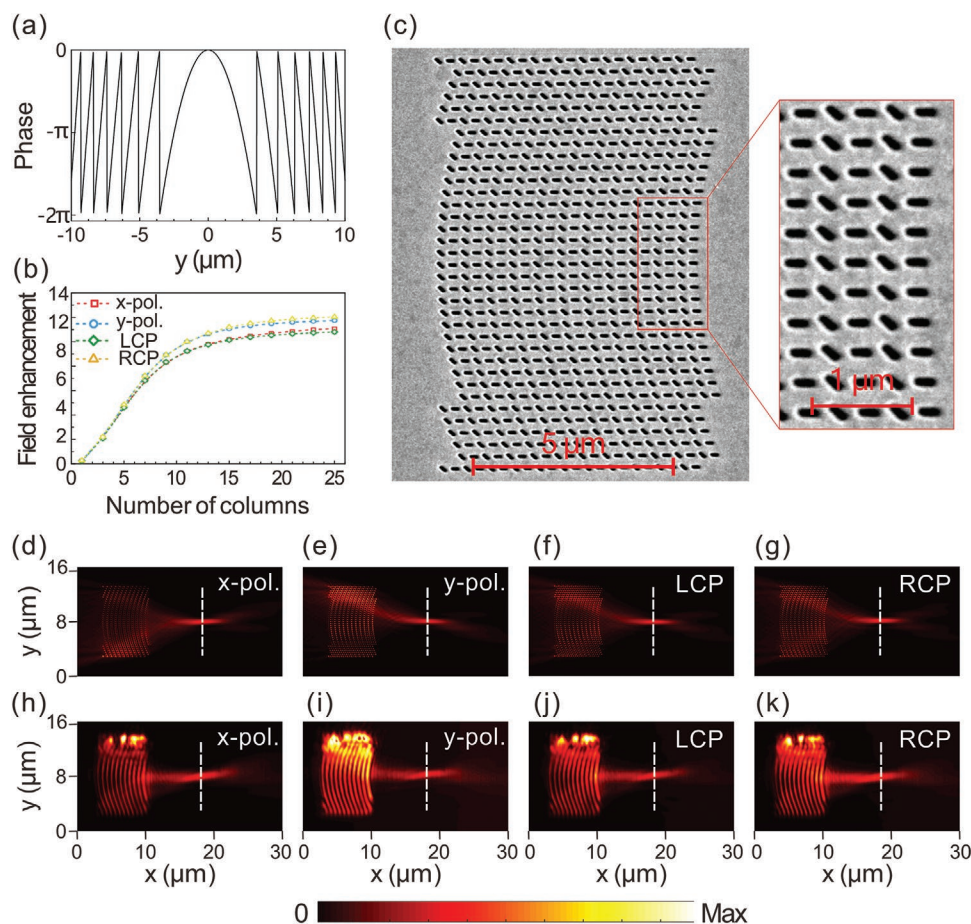


Figure 4. a) The phase profile required for near-field focusing with $f = 10 \mu\text{m}$. b) Simulated electric field intensity enhancement versus the number of nanoslit column pairs. c) SEM image of the sample for near-field focusing. d–k) Simulated (d–g) and NSOM-measured (h–k) electric field intensity distributions for the d,h) x-polarized, e,i) y-polarized, f,j) LCP, and g,k) RCP incidences, respectively. White dashed lines in (d–k) show the positions of the focal points.

that with one pair of nanoslit column. The fabricated sample is shown in Figure 4c. The simulated and experimental results in Figure 4d–k clearly demonstrate light waves of different polarizations will be focused at the same point, and the simulation results agree well with the measured results. The extracted focal lengths are all $\approx 8.3 \mu\text{m}$, being smaller than the theoretical value due to the finite size of the plasmonic lens. The field intensity profiles along the white dashed lines in Figure 4d–k can be found in Figure S7a–d, Supporting Information. The extracted focusing spot size under the four incident polarizations are all comparable to one wavelength of the SPs, implying highly focusing effect is achievable.

The “lossless” SP beams preserve the nondiffracting characteristic of cosine-Gauss beams, while compensating the intrinsic propagation loss of the SPs within a certain range.^[20] They suggest potential applications in on-chip transmission and nondiffractive plasmon optics. The phase profile for “lossless” plasmon beams along the y direction should follow

$$\frac{dy}{dx} \exp \left[\gamma/l \left(\frac{\lambda_{\text{spp}}}{2\pi} \frac{\partial \phi(y)}{\partial x} \right) \right] = c \quad (13)$$

where l represents the attenuation length of SPs, and c is a constant. The phase profile desired for “lossless” plasmon beams is plotted in Figure 5a, which can be realized with the same approach for near-field focusing above-mentioned, and the lateral distances used for each column along the y direction can be seen in Figure S8, Supporting Information. Again, the field enhancement of “lossless” plasmon beams increases with the number of nanoslit column pairs along the x direction (Figure 5b), but finally approaches a constant value. Here the field enhancement is defined as the ratio of the average electric field intensity of SPs in the range of 5–15 μm away from the rightmost nanoslits to that of the incident light. By taking 13 pairs of the nanoslit column, we have successfully fabricated the sample (Figure 5c) and measured the characteristics of the “lossless” plasmon beams under different incident polarizations. In this case, the field intensity has 44-fold increase, in contrast to that with one pair of nanoslit column. Figure 5d–k presents the simulated and experimentally measured “lossless” plasmon beams under the four incident polarizations. The intensity profiles of the main lobes demonstrate a preserved value within ≈ 0 –30 μm distance under different polarization states (see Figure S9a–d, Supporting Information). The simulated and

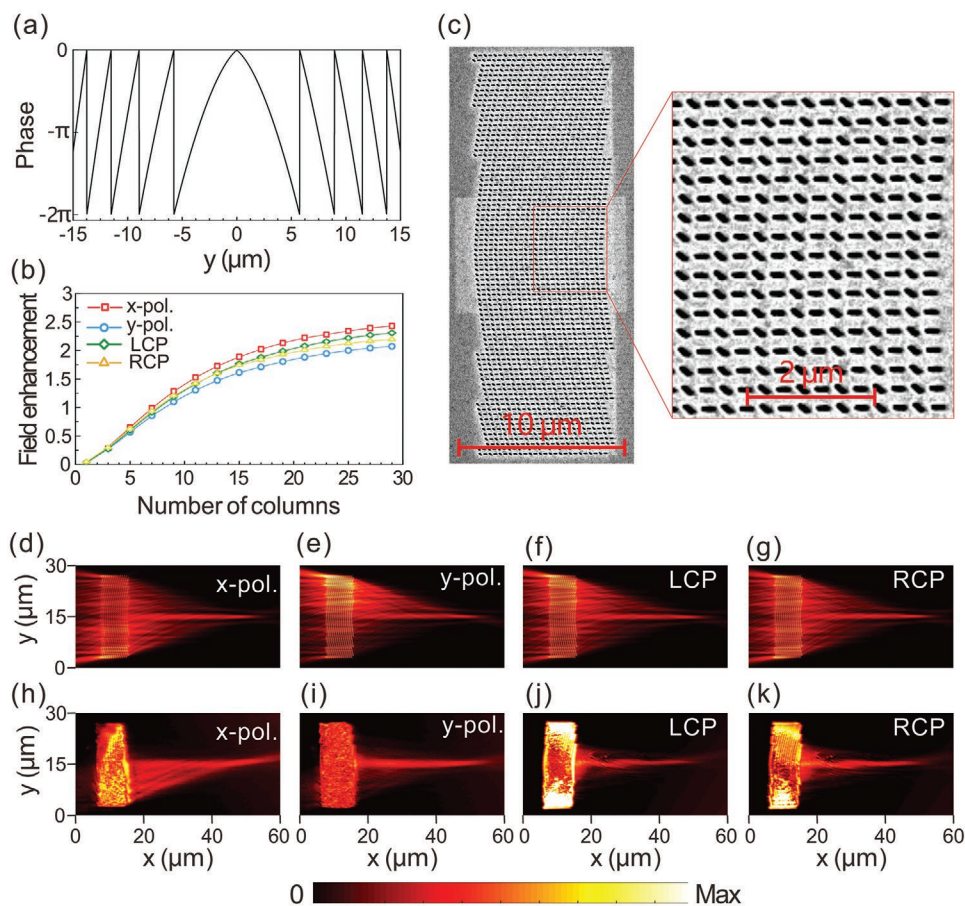


Figure 5. a) The phase profile required for “lossless” plasmon beams with $c = 0.03$. b) Simulated electric field intensity enhancement versus the number of nanoslit column pairs. c) SEM image of the sample for “lossless” plasmon beams. d–k) Simulated (d–g) and NSOM-measured (h–k) electric field intensity distributions for the d,h) x-polarized, e,i) y-polarized, f,j) LCP, and g,k) RCP incidences, respectively.

experimental results are in good accordance. The experimentally demonstrated “lossless” beam distance of $30 \mu\text{m}$ is close to that in a previous work,^[20] and may find potential applications, such as on-chip optical interconnects and optical tweezers.

It is worth emphasizing that the number of nanoslit column pairs for the three fabricated samples is chosen by considering the fabrication complexity and SP intensity. The resultant SP field can be made close to the maximum value by use of 17, 11, and 13 pairs of nanoslit columns, respectively, with which the FIB etching resolution does not reduce. We have simulated the electric field intensity distributions of plasmonic Airy beams, near-field focusing, and “lossless” beams when the three devices are excited by arbitrary polarization states, such as 45° linear polarization and three elliptical polarizations (see Figure S10, Supporting Information). The simulated results demonstrate that the expected plasmonic field intensity distributions can still occur under these polarization states, which further validates the performance of polarization independence. It should be emphasized here that although the designed devices can operate regardless of the polarization state, i.e., the generated plasmonic beam patterns for different polarization excitations can overlap for each metadvice, the coupling efficiencies for different polarization excitations can be somewhat different (see the calculated coupling efficiencies for the three devices

under the x and y polarizations, LCP, and RCP incidences in Table S1, Supporting Information). The reason that causes different coupling efficiencies is attributed to the fact that our design strategy is merely based on the excited SPs propagating along the x direction, while the contribution from the excited SPs propagating along the y direction is ignored. However, the later branch of excited SPs propagating along the y direction will be inevitably scattered by the nanoslits when they propagate along the y direction, which thus contributes to the SP field in the observation regions. Although this portion of SP field takes up a small proportion of light energy in the observation regions, it differs from different polarization excitations. Consequently, the actual coupling efficiencies are more or less dependent on the polarization state.

Finally, it is important to illustrate the factors that cause the deviation between the simulation and experiment for the aforementioned three functionalities. The deviation mainly originates from imperfect fabrication of the nanoslits arising from FIB etching, and NSOM measurement. In the NSOM measurement, the big probe aperture and the vibration also result in some differences. In addition, the charge-coupled device (CCD) is put along the reflected light path to help us to find the sample so as to ensure the incident beam illuminates the nanoslit region. These optical elements in the region bounded

by the rectangle shown in Figure 3e are fastened. We, therefore, have to adjust the laser beam direction to guarantee the light waves reflected by the sample reach the CCD. Actually, the incident beam upon the sample is not absolutely vertical to the metallic surface, and has an angle of $\approx 5^\circ$ with respect to the normal incidence in the NSOM measurement. If the incident light has an oblique angle to the normal direction of the metallic surface, the generated plasmon beam quality reduces with the increase of the incidence angle since the amplitude and phase distributions of SPs do not fully follow the required conditions (see Figures S11–S13, Supporting Information).^[32]

3. Conclusion

In conclusion, we have proposed a strategy for constructing a polarization-independent plasmonic metasurfaces based on double-lined metallic nanoslits. The presented metasurface scheme not only can couple spatial light waves into SPs under arbitrary polarization states, but also can independently modulate the amplitude and phase of the generated SPs. We can, thus, flexibly manipulate the wavefront of the SPs for various potential applications, regardless of the incident polarization state. The plasmonic metasurfaces for polarization-independent plasmonic Airy beams, near-field focusing, and intensity-preserved “lossless” beams have been designed, fabricated, and experimentally characterized at 633 nm. The NSOM measurement results are well consistent with the simulated results, and validate the generation of high-performance plasmon beams. These results may pave a meaningful step toward exploration of high-performance polarization-independent plasmon devices based on plasmonic metasurfaces.

Supporting Information

Supporting Information is available from the Wiley Online Library or from the author.

Acknowledgements

This work was supported by the National Major Research and Development Program (grant nos. 2018YFB2200200 and 2017YFA0205700) and the National Natural Science Foundation of China (grant nos. 11474116, 11674118, 61922082, 61875223, and 21790364). The support from the Vacuum Interconnected Nanotech Workstation (Nano-X) of Suzhou Institute of Nano-Tech and Nano-Bionics (SINANANO), Chinese Academy of Sciences is also acknowledged. The authors thank engineer Wei Xu in the Center of Optoelectronic Micro/Nano Fabrication and Characterizing Facility of WNLO for the support in electron-beam vapor deposition technology.

Conflict of Interest

The authors declare no conflict of interest.

Keywords

metasurfaces, polarization-independent devices, surface plasmons, wavefronts

Received: May 28, 2020
Revised: August 16, 2020
Published online:

- [1] W. L. Barnes, A. Dereux, T. W. Ebbesen, *Nature* **2003**, 424, 824.
- [2] T. Yang, H. Lin, B. Jia, *Front. Optoelectron.* **2018**, 11, 2.
- [3] C. Wan, G. Rui, J. Chen, Q. Zhan, *Front. Optoelectron.* **2019**, 12, 88.
- [4] A. Minovich, A. E. Klein, N. Janunts, T. Pertsch, D. N. Neshev, Y. S. Kivshar, *Phys. Rev. Lett.* **2011**, 107, 116802.
- [5] A. E. Klein, A. Minovich, M. Steinert, N. Janunts, A. Tünnermann, D. N. Neshev, Y. S. Kivshar, T. Pertsch, *Opt. Lett.* **2012**, 37, 3402.
- [6] N. Yu, F. Capasso, *Nat. Mater.* **2014**, 13, 139.
- [7] H.-T. Chen, A. J. Taylor, N. Yu, *Rep. Prog. Phys.* **2016**, 79, 076401.
- [8] J. Lin, J. P. B. Mueller, Q. Wang, G. Yuan, N. Antoniou, X.-C. Yuan, F. Capasso, *Science* **2013**, 340, 331.
- [9] X. Zhang, Y. Xu, W. Yue, Z. Tian, J. Gu, Y. Li, R. Singh, S. Zhang, J. Han, W. Zhang, *Adv. Mater.* **2015**, 27, 7123.
- [10] Q. Xu, X. Zhang, Q. Yang, C. Tian, Y. Xu, J. Zhang, H. Zhao, Y. Li, C. Ouyang, Z. Tian, J. Gu, X. Zhang, J. Han, W. Zhang, *Optica* **2017**, 4, 1044.
- [11] L. Li, T. Li, S. M. Wang, C. Zhang, S. N. Zhu, *Phys. Rev. Lett.* **2011**, 107, 126804.
- [12] E.-Y. Song, S.-Y. Lee, J. Hong, K. Lee, Y. Lee, G.-Y. Lee, H. Kim, B. Lee, *Laser Photonics Rev.* **2016**, 10, 299.
- [13] S. Wang, X. Wang, Y. Zhang, *Opt. Express* **2017**, 25, 23589.
- [14] X. Yin, L. Chen, X. Li, *Opt. Express* **2018**, 26, 23251.
- [15] Y. Gorodetski, A. Niv, V. Kleiner, E. Hasman, *Phys. Rev. Lett.* **2008**, 101, 043903.
- [16] S.-Y. Lee, K. Kim, S.-J. Kim, H. Park, K.-Y. Kim, B. Lee, *Optica* **2015**, 2, 6.
- [17] S.-Y. Lee, K. Kim, G.-Y. Lee, B. Lee, *Opt. Express* **2015**, 23, 15598.
- [18] G. Li, Y. Sun, S. Wang, *Nanoscale Res. Lett.* **2019**, 14, 156.
- [19] J. Lin, J. Dellinger, P. Genevet, B. Cluzel, F. de Fornel, F. Capasso, *Phys. Rev. Lett.* **2012**, 109, 093904.
- [20] L. Li, T. Li, S. M. Wang, S. N. Zhu, *Phys. Rev. Lett.* **2013**, 110, 046807.
- [21] S. Wang, S. Wang, Y. Zhang, *Opt. Express* **2018**, 26, 5461.
- [22] X. Zhao, X. Feng, P. Zhao, F. Liu, K. Cui, W. Zhang, Y. Huang, *Opt. Express* **2019**, 27, 22053.
- [23] H. Kim, J. Park, S.-W. Cho, S.-Y. Lee, M. Kang, B. Lee, *Nano Lett.* **2010**, 10, 529.
- [24] Q. Tan, Q. Guo, H. Liu, X. Huang, S. Zhang, *Nanoscale* **2017**, 9, 4944.
- [25] W.-Y. Tsai, Q. Sun, G. Hu, P. C. Wu, R. J. Lin, C.-W. Qiu, K. Ueno, H. Misawa, D. P. Tsai, *Adv. Opt. Mater.* **2019**, 7, 1801060.
- [26] Y. Zhang, X. Zeng, L. Ma, R. Zhang, Z. Zhan, C. Chen, X. Ren, C. He, C. Liu, C. Cheng, *Adv. Opt. Mater.* **2019**, 7, 1900372.
- [27] M. V. Berry, N. L. Balazs, *Am. J. Phys.* **1979**, 47, 264.
- [28] G. A. Siviloglou, J. Broky, A. Dogariu, D. N. Christodoulides, *Phys. Rev. Lett.* **2007**, 99, 213901.
- [29] G. A. Siviloglou, D. N. Christodoulides, *Opt. Lett.* **2007**, 32, 979.
- [30] J. Baumgartl, M. Mazilu, K. Dholakia, *Nat. Photon.* **2008**, 2, 675.
- [31] M. Righini, A. S. Zelenina, C. Girard, R. Quidant, *Nat. Phys.* **2007**, 3, 477.
- [32] Y. Sonnefraud, S. Kerman, G. Di Martino, D. Y. Lei, S. A. Maier, *Opt. Express* **2012**, 20, 4893.